Reaction Kinetics, Mechanisms and Catalysis
https://doi.org/10.1007/s11144-024-02682-2

Metallic silver modified SnO_2–Zn_2SnO_4 cube nanomaterials for improved photocatalytic degradation of rhodamine B

Shuyun Huang[1] · Huanhuan Xu[1] · Yue Ouyang[1] · Yun Zhou[1] · Junwei Xu[2] · Jianjun Liu[1]

Received: 15 May 2024 / Accepted: 5 July 2024

Abstract

To modify the wide bandgap and intrinsic high recombination rate of photogenerated charge carriers of Zn_2SnO_4 photocatalysts, Ag/SnO_2–Zn_2SnO_4 composites were prepared by depositing Ag nanoparticles onto cube-shaped SnO_2–Zn_2SnO_4 nanomaterials via photoreduction. The composites were characterized by XRD, SEM, EDS, TEM, XPS, and UV–Vis DRS, and their photocatalytic degradation effect on rhodamine B (Rh B) for different Ag loadings was studied, with 10%Ag/SnO_2–Zn_2SnO_4 showing the greatest effect. The UV photocatalytic degradation rate of the Rh B solution reaches 100% after 12 min of visible light irradiation and 91% after five cycles. The free radical trapping agent experiment indicated that the active substances of Ag/SnO_2–Zn_2SnO_4 photocatalysis are $\cdot O_2^-$ and h^+. Further, photoelectrochemical tests revealed the higher electron–hole separation efficiency and faster charge transfer rate of the composites, enhancing the formation of photoproduced carriers and photocatalytic activity.

Keywords SnO_2 · Zn_2SnO_4 · Photocatalysis · Rhodamine B · Mechanism

Introduction

Owing to rapid economic development and population growth, environmental pollution has become an increasingly serious concern [1]. Nearly 2 million tons of waste pollutants are discharged into the Yangtze River Basin every day, which is not only damaging to the ecological environment but also poses a serious threat to human health [2–4]. Traditional sewage treatment methods, including adsorption [5], membrane separation [6], ion exchange [7], and electrochemical

✉ Jianjun Liu
JianjunLiu_pxu@163.com

[1] School of Materials and Chemical Engineering, Pingxiang University, Pingxiang 337055, China

[2] Department of Applied Chemistry, Jiang Xi Academy of Sciences, Nanchang 330096, China

Published online: 30 July 2024

purification [8], present some limitations, such as low adsorption rates, high costs, secondary pollution, and high energy consumption. In recent years, photocatalytic degradation techniques have gained significant attention owing to their low costs, rapid degradation effects, and environmental friendliness [9, 10]. Tin dioxide (SnO_2) is a commonly used photocatalytic semiconductor material because of its cost-effectiveness, environmental safety, nontoxicity, and chemical stability [11–13]. However, it has a large bandgap and narrow light absorption range and exhibits poor transfer and separation of photogenerated carriers. Several methods have been developed to enhance the photoresponse of wide-bandgap photocatalysts and improve the separation efficiency of photogenerated electrons and holes, including ion doping [14, 15], morphological control [16, 17], and semiconductor recombination [18–22].

Zinc stannate (Zn_2SnO_4) is an n-type oxide semiconductor with a wide bandgap (3.0–3.9 eV), high electrical conductivity, high electron mobility, advantageous optical properties, and high chemical stability [23–26]. Nevertheless, its photocatalytic efficiency is inhibited by the poor absorption of visible light and rapid recombination of photogenerated carriers. In this regard, heterojunction photocatalysts offer an effective means to improve the poor photoresponse of a single semiconductor and the low separation efficiency of electron–hole pairs, as revealed in different studies. For example, in their synthesis of SnO_2–Zn_2SnO_4/graphene composite photocatalysts via a hydrothermal method, Li et al. [27] showed that graphene can effectively transfer photogenerated electrons from the conduction band of Zn_2SnO_4, delay the recombination of carriers, and improve photocatalytic activity. Further, Zou et al. [28] synthesized Zn_2SnO_4 quantum dots/Bi_2WO_6 nanocomposites using a two-step hydrothermal approach and investigated their photocatalytic activity for gaseous acetone under visible light irradiation. The improved absorption of visible light and separation efficiency of photogenerated carriers were attributed to the heterojunction structure of the nanocomposites.

Considering that the energy band structures of SnO_2 and Zn_2SnO_4 match, SnO_2–Zn_2SnO_4 can form a Z-scheme heterojunction; this, however, does not provide the satisfactory separation of photogenerated carriers. In addition to the construction of the heterojunction, the surface plasmon resonance (SPR) effect of noble metal nanoparticles can increase the absorption of visible light, and their Fermi level can promote electron transfer [29–33]. Thus, noble metal modification is also considered effective in elevating the photocatalytic performance of semiconductors. Lu et al. [34] synthesized Ag/Zn_2SnO_4 photocatalysts using a one-cloth hydrothermal method; these effectively improved the separation efficiency of photoproduced electron–hole pairs, thus enhancing the photocatalytic performance of methyl orange. In another study, Liu et al. [35] prepared Ag/SnO_{2-x}/$Bi_4O_5I_2$ ternary composites and studied the photocatalytic degradation of antibiotics and inactivation of bacteria; the composites promoted the transfer of photogenerated charge carriers and reduced the recombination of electron–hole pairs.

In this study, cube-shaped SnO_2–Zn_2SnO_4 nanomaterials were synthesized by precipitation, and Ag/SnO_2–Zn_2SnO_4 ternary composite photocatalysts were then prepared by depositing Ag nanoparticles onto the nanomaterial surface via photoreduction. Rhodamine B (Rh B) was used as a model pollutant to

investigate the photocatalytic degradation effect and reaction mechanism of the Ag/SnO_2–Zn_2SnO_4 composites.

Experimental methods

Preparation of SnO_2–Zn_2SnO_4

All chemicals and solvents used herein were supplied by Sinopharm Reagent Co., Ltd. (China). The cube-shaped SnO_2–Zn_2SnO_4 nanomaterials were prepared as follows. First, 1 mmol $SnCl_4{\cdot}5H_2O$ (AR) and 1 mmol $ZnCl_2$ (AR) were dispersed in 40 mL of water under vigorous stirring for 30 min. Then, 10 mL of NaOH (10 M) was added, and the solution was stirred for a further 30 min. More NaOH (10 mL) was subsequently added to the above solution and stirred for 2 h. The resultant white precipitate was separated by centrifugation, washed with water and ethanol, and then dried at 80 °C for 12 h. The dried samples were calcinated in air for 30 min at 850 °C to yield the SnO_2–Zn_2SnO_4 nanomaterials.

Preparation of Ag/SnO_2–Zn_2SnO_4

First, 100 mg of the SnO_2–Zn_2SnO_4 sample was dispersed in 40 mL of water for 1 h using an ultrasonic bath. Different amounts of $AgNO_3$ solution were then added to the SnO_2–Zn_2SnO_4 dispersion solution, and the mixtures were stirred vigorously for 1 h under irradiation from a xenon lamp (220 W). The products obtained by centrifugation were washed several times and then dried at 80 °C for 12 h. The Ag/SnO_2–Zn_2SnO_4 composites were labeled according to the mass fraction of Ag (5, 10, 15, and 20%) as 5%Ag/SnO_2–Zn_2SnO_4, 10%Ag/SnO_2–Zn_2SnO_4, 15%Ag/SnO_2–Zn_2SnO_4, and 20%Ag/SnO_2–Zn_2SnO_4.

Photodegradation testing and characterization

Details about the equipment, operation conditions, and experimental processes and parameters are provided in the supplementary material.

Results and discussion

X-ray diffraction analysis

Fig. 1 shows the XRD patterns of SnO_2–Zn_2SnO_4 and Ag/SnO_2–Zn_2SnO_4. The diffraction peaks at 17.72°, 29.14°, 34.29°, 35.91°, 41.68°, 55.11°, and 60.44° belong to the (111), (220), (311), (222), (400), (511), and (440) crystal planes (hkl) of Zn_2SnO_4 [36]. The diffraction peaks at 26.61° and 51.78° are ascribed to the (111) and (211) crystal planes of SnO_2 [37]. All the SnO_2–Zn_2SnO_4 peaks correspond well with standard Zn_2SnO_4 (JCPDS card no. 24-1470) and SnO_2 (JCPDS card no.

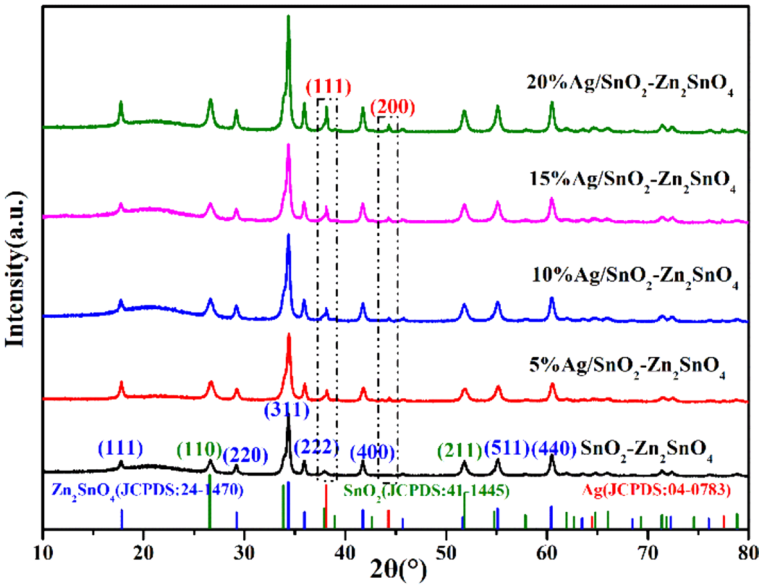

Fig. 1 XRD patterns of the SnO_2–Zn_2SnO_4 and Ag/SnO_2–Zn_2SnO_4 composites. The experimental conditions include a tube voltage of 40 kV, a tube current of 30 mA, a Cu K_α radiation source, and a scanning step of 2° min^{-1}

41-1445) diffraction data. Compared with the case for the SnO_2–Zn_2SnO_4 composite, the diffraction peak of Ag/SnO_2–Zn_2SnO_4 is enhanced at 38.02°, and a new peak appears at 44.27°; these belong to the (111) and (200) crystal planes of metallic Ag (JCPDS card no. 04-0783) [38]. Moreover, the peaks at 38.02° and 44.27° gradually increase in intensity with increasing Ag content, confirming that the Ag nanoparticles exist in the form of metallic Ag on the Ag/SnO_2–Zn_2SnO_4 surface.

SEM and EDS analysis

Fig. S1 shows the SEM images of the synthesized samples. The SnO_2–Zn_2SnO_4 nanomaterials exhibit cubic morphology, a three-dimensional appearance, and a relatively uniform particle size. At an Ag content of 5%, only a few Ag nanoparticles are present on the SnO_2–Zn_2SnO_4 surface, as shown in Fig. S1b; with the increase in the Ag content, the Ag nanoparticle coverage on the nanomaterial surface increases, as shown in Fig. S1c–e. Furthermore, the increase in the Ag nanoparticle loading leads to agglomeration on the nanomaterial surface.

Figs. S2 and S3 depict the EDS compositional maps of SnO_2–Zn_2SnO_4 and 10%Ag/SnO_2–Zn_2SnO_4. O, Sn, and Zn can be detected in SnO_2–Zn_2SnO_4 (Fig. S1), and O, Sn, Zn, and Ag can be noted in 10%Ag/SnO_2–Zn_2SnO_4 (Fig. S3) with a uniform distribution.

TEM analysis

The morphology and structure of the 10%Ag/SnO_2–Zn_2SnO_4 composite samples were further examined by TEM. As depicted in Fig. 2a, 10%Ag/SnO_2–Zn_2SnO_4 exhibits a cubic shape, consistent with the SEM results. As shown in Fig. 2b, the crystal lattice contains streaks with spacings of 0.500, 0.335, and 0.236 nm, corresponding to the (111) planes of Zn_2SnO_4 [39], the (110) planes of SnO_2 [40], and the (111) planes of metallic Ag [41]. Fig. 2c displays the selected area electron diffraction (SAED) results; the four distinct diffraction rings correspond to the (110) planes of SnO_2, (111) planes of the Ag nanoparticles, and (311) and (511) planes of Zn_2SnO_4, consistent with the HRTEM results. In addition to the crystal faces of SnO_2 and Zn_2SnO_4, the (111) crystal faces of metallic Ag can be observed, consistent with the XRD results.

XPS analysis

XPS was employed to evaluate the surface chemical states of the catalysts. The Zn 2*p* spectra in Fig. 3a show two prominent peaks at around 1021.7 and 1044.8 eV, which are assigned to Zn $2p_{3/2}$ and Zn $2p_{1/2}$ [42]. Comparing the X-ray photoelectron spectra of SnO_2–Zn_2SnO_4 and 10%Ag/SnO_2–Zn_2SnO_4, the Zn 2*p* peaks do not shift. Fig. 3b depicts Sn 3*d* peaks at around 486.3 eV (Sn $3d_{5/2}$) and 494.6 eV (Sn $3d_{3/2}$) for SnO_2–Zn_2SnO_4 [43]. However, the Sn $3d_{5/2}$ and $3d_{3/2}$ binding energies of 10%Ag/SnO_2–Zn_2SnO_4 shift to higher values 486.5 and 494.8 eV increasing by 0.2 eV compared with those for SnO_2–Zn_2SnO_4. These shifts may indicate the formation of SnO_2 resulting from the charge reassignment [27]. In the Ag 3d spectra in Fig. 3c, two symmetrical peaks can be observed at around 367.5 and 373.5 eV, which are assigned to Ag $3d_{5/2}$ and Ag $3d_{3/2}$ of metallic Ag [44], consistent with the XRD and TEM results. As displayed in Fig. 3d, the O 1*s* spectrum displays characteristic peaks at around 530.3, 531.6, and 533.5 eV, corresponding to surface lattice oxygen (O^{2-}), peroxide (O_2^{2-}), and superoxide (O_2^-) species [45]. The superoxide species of the 10%Ag/SnO_2–Zn_2SnO_4 sample exhibits a significantly higher peak

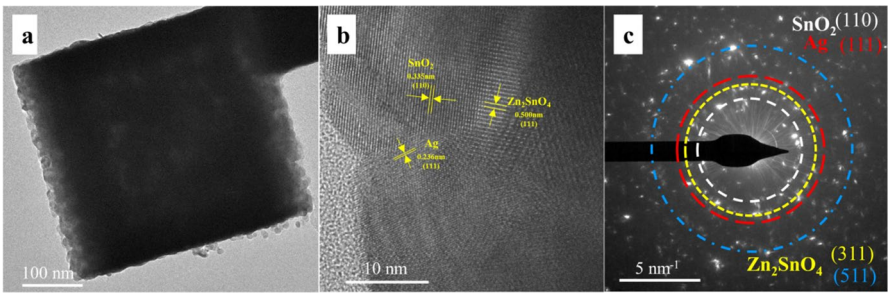

Fig. 2 **a** TEM, **b** HRTEM, and **c** SAED images of the 10%Ag/SnO_2–Zn_2SnO_4 samples. The experimental conditions include a working voltage of 200 kV

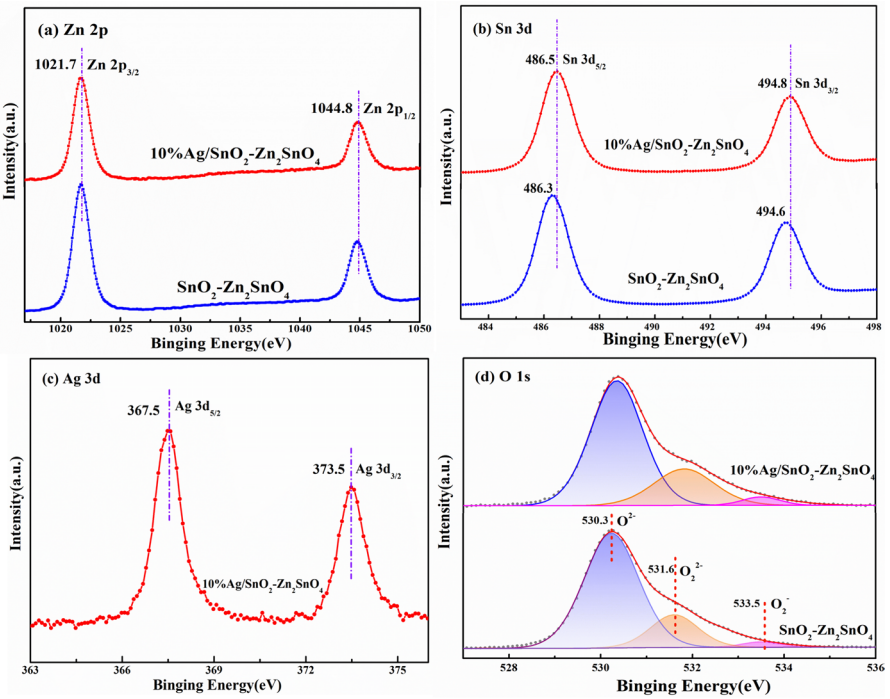

Fig. 3 XPS analysis of the SnO_2–Zn_2SnO_4 and 10%Ag/SnO_2–Zn_2SnO_4 samples: **a** Zn 2*p*, **b** Sn 3*d*, **c** Ag 3*d*, and **d** O 1*s* spectra. The experimental conditions include an Al Kα X-ray source ($h\nu = 1486.6$ eV), a filament current of 6 mA, and a working voltage of 12 kV; the C 1*s* peak of graphite at 284.6 eV was used as a standard

than that of SnO_2–Zn_2SnO_4, indicating that the addition of metallic Ag is more conducive to superoxide formation on the surface of the catalyst.

Optical properties

Fig. 4 depicts the UV–Vis absorption spectra of the samples. As shown in Fig. 4a, SnO_2–Zn_2SnO_4 exhibits strong absorption in the UV region owing to the wide bandgap of SnO_2 and Zn_2SnO_4; the Ag/SnO_2–Zn_2SnO_4 species also exhibit significantly higher absorption intensities in this region. Moreover, the Ag/SnO_2–Zn_2SnO_4 samples display significant absorption peaks in the range of 400–500 nm due to the SPR of the Ag nanoparticles [46]. The Kubelka–Munk function was used to calculate the bandgap energies (E_g) of the catalysts, as shown in Eq. 1:

$$(\alpha h\nu)^{1/n} = A\left(h\nu - E_g\right) \tag{1}$$

Here: α is the absorption coefficient, h is Planck's constant, ν is the optical frequency, A is the proportionality constant, and n is a variable that depends on the characteristics of the semiconductor material.

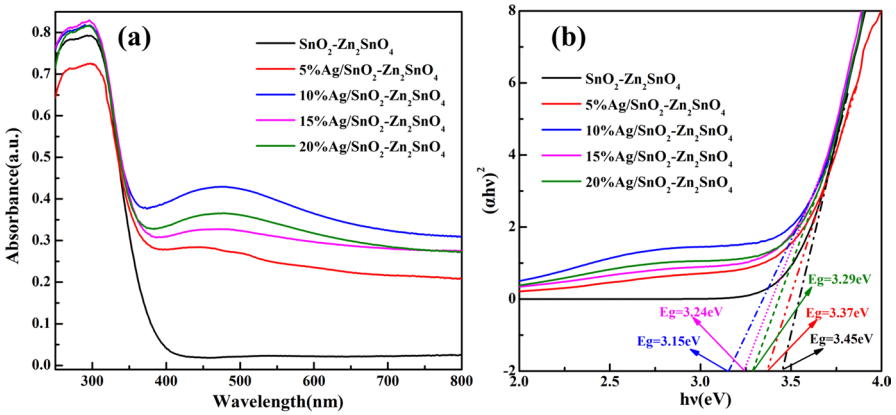

Fig. 4 **a** UV–Vis absorption spectra (wavelength range: 250–800 nm) and **b** bandgap plots

Fig. 4b depicts the bandgaps of the catalysts. The optical bandgap widths of SnO_2–Zn_2SnO_4, 5%Ag/SnO_2–Zn_2SnO_4, 10%Ag/SnO_2–Zn_2SnO_4, 15%Ag/SnO_2–Zn_2SnO_4, and 20%Ag/SnO_2–Zn_2SnO_4 are 3.45, 3.37, 3.15, 3.24, and 3.29 eV. Notably, 10%Ag/SnO_2–Zn_2SnO_4 has the smallest bandgap; this is conducive to the transition of electrons from the valence band to the conduction band during excitation and the creation of photogenerated electrons and holes, which may, therefore, help improve its photocatalytic activity.

Photocatalytic activity

Fig. 5 shows the UV degradation effect on the Rh B solution and its kinetic behavior using different photocatalysts under visible light irradiation. As shown in Fig. 5a, in the absence of a photocatalyst, the Rh B solution is stable under irradiation,

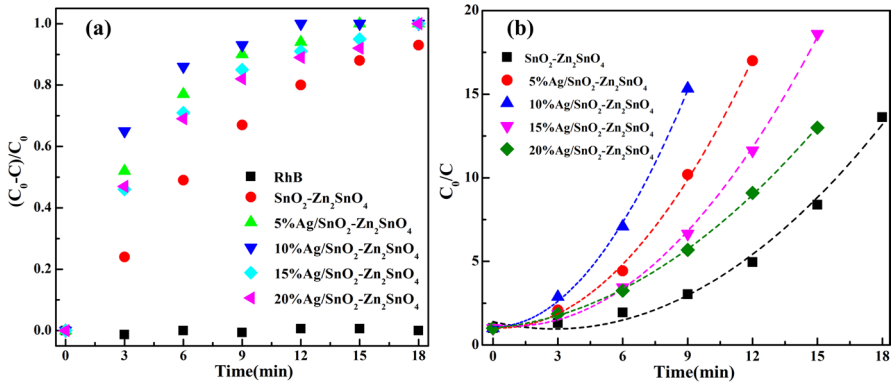

Fig. 5 **a** Photocatalytic degradation rate of Rh B and **b** the kinetic behavior of photocatalytic degradation. The experimental conditions include irradiation from a xenon lamp (300 W), a Rh B solution concentration of 20 mg/L, and a photocatalyst content of 100 mg

and its self-degradation is negligible. However, the Rh B degradation rate with SnO_2–Zn_2SnO_4 reaches 93% after 18 min of irradiation. The photocatalytic performance of SnO_2–Zn_2SnO_4 supported with Ag nanoparticles is further enhanced, especially in the case of 10%Ag/SnO_2–Zn_2SnO_4, reaching 100% after 12 min of irradiation. The total organic carbon (TOC) content of the Rh B solution was tested to determine whether the photocatalyst had a bleaching or mineralizing effect on the solution. The TOC content of 20 mg/L Rh B is 786.7 μg/L; after reacting with 10%Ag/SnO_2–Zn_2SnO_4 for 12 min, the TOC of the solution decreases to 471.9 μg/L, and the total mineralization rate is 60%. The experimental results indicate that the Rh B solution can be mineralized into small inorganic molecules by the photocatalysts.

The kinetic behavior of photocatalytic degradation was fitted using the nonlinear least squares method, as shown in Fig. 5b. Table S1 presents the degradation rate and standard errors of the photocatalysts. The rate constants for the degradation of the Rh B solutions by SnO_2–Zn_2SnO_4, 5%Ag/SnO_2–Zn_2SnO_4, 10%Ag/SnO_2–Zn_2SnO_4, 15%Ag/SnO_2–Zn_2SnO_4, and 20%Ag/SnO_2–Zn_2SnO_4 are 0.1389, 0.2426, 0.3086, 0.2024, and 0.1793 min^{-1}. The rate constant of 10%Ag/SnO_2–Zn_2SnO_4 is more than twofold higher than that of SnO_2–Zn_2SnO_4, indicating that the addition of Ag nanoparticles enhances the photocatalytic performance.

The stability of the photocatalysts after repeated applications is a key measure of their performance. As shown in Fig. S4, the photocatalytic Rh B degradation efficiency of 10%Ag/SnO_2–Zn_2SnO_4 reaches 91% after five cycles, indicating the high stability of the composite.

To assess the photocatalytic mechanism of the Ag/SnO_2–Zn_2SnO_4 composites, 10%Ag/SnO_2–Zn_2SnO_4 was selected for conducting the active material capture experiment. Isopropyl alcohol (IPA, 1.5 mmol/L), disodium ethylenediamine tetraacetate (Na_2EDTA, 1.5 mmol/L), and *p*-benzoquinone (BQ, 1.5 mmol/L) were used to capture hydroxyl radicals (·OH), holes (h^+), and superoxide radicals ($\cdot O_2^-$). As shown in Fig. 6, IPA causes a small decrease in the degradation of Rh B, indicating that ·OH does not have a significant effect on the reaction. When Na_2EDTA is added to the reaction system, the degradation rate of Rh B decreases more significantly, indicating the presence of photogenic holes in the reaction solution. When BQ is added to the photocatalytic reaction, the degradation of Rh B is the lowest. Thus, $\cdot O_2^-$ has a greater influence on the reaction and plays a major role in the reaction system. Overall, the main active substances in the photocatalytic degradation of Rh B using 10%Ag/SnO_2–Zn_2SnO_4 are $\cdot O_2^-$ and h^+, while the secondary active substance is ·OH.

Photoelectric properties

To further validate the generation, separation, and transfer of photogenic carriers in photocatalysis, transient photocurrent responses and Nyquist plots were used to analyze the photoelectric properties of SnO_2–Zn_2SnO_4 and the Ag/SnO_2–Zn_2SnO_4 composites for different Ag loadings (5, 10, 15, and 20%). Fig. 7a shows the transient photocurrent responses of SnO_2–Zn_2SnO_4 and Ag/SnO_2–Zn_2SnO_4 under irradiation from a xenon

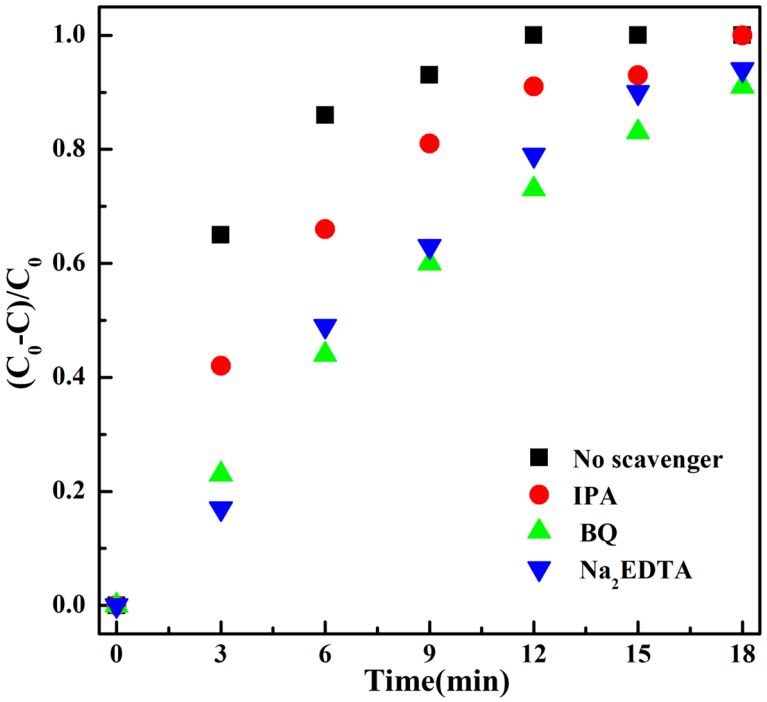

Fig. 6 Photocatalytic activity using different quenching materials. The experimental conditions include irradiation from a xenon lamp (300 W), a Rh B solution concentration of 20 mg/L, and a photocatalyst content of 100 mg

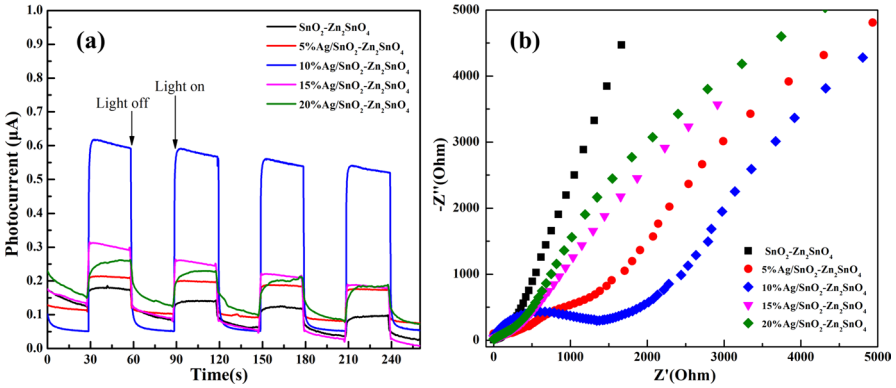

Fig. 7 **a** Transient photocurrent response of the catalysts at a voltage of 0.8 V and using xenon light every 30 s, and **b** electrochemical impedance spectra of the catalysts with a frequency range of 100 kHz to 0.1 Hz. The experimental conditions include a Na_2SO_4 solution concentration of 0.2 mol/L

lamp with repeated on–off switching. As shown in Fig. 7a, the photocurrent of the 10%Ag/SnO_2–Zn_2SnO_4 catalyst is the highest among the tested materials, indicating that its photogenic charge recombination rate is the lowest. The electrochemical impedance spectra in Fig. 7b reveal that 10%Ag/SnO_2–Zn_2SnO_4 has the smallest semicircle diameter, representing the fastest interfacial charge carrier transfer rate [47]. Therefore, it is plausible that the presence of metallic Ag in the Ag/SnO_2–Zn_2SnO_4 composite can effectively lead to the separation of electron–hole pairs and improve the transmission efficiency of photoproduced carriers.

To investigate the band structure of the Ag/SnO_2–Zn_2SnO_4 heterojunction, the band structures of SnO_2–Zn_2SnO_4 and 10%Ag/SnO_2–Zn_2SnO_4 were explored through Mott–Schottky (M–S) curves at different frequencies, as displayed in Fig. 8a and b. The positive slopes of the M–S curves for SnO_2–Zn_2SnO_4 are typical of n-type semiconductors. Moreover, the conduction band edge potential (ECB) values of SnO_2–Zn_2SnO_4 and 10%Ag/SnO_2–Zn_2SnO_4, obtained via extrapolation of the M–S curves to the x-axis, are approximately − 1.14 and − 0.20 eV. The lower ECB of 10%Ag/SnO_2–Zn_2SnO_4 compared to SnO_2–Zn_2SnO_4 indicates that the former can help improve the utilization efficiency of photogenerated charge carriers and enhance the photocatalytic activity against organic pollutants, consistent with the photocatalytic degradation of Rh B.

Proposed photocatalytic reaction mechanism

A photocatalytic reaction mechanism was proposed for the Ag/SnO_2–Zn_2SnO_4 composite based on the experimental and characterization results. First, the valence band (VB) and conduction band (CB) potentials of the SnO_2 and Zn_2SnO_4 catalysts were estimated according to Eqs. 2 and 3 [48]:

$$E_{VB} = X - E_e - 0.5E_g \tag{2}$$

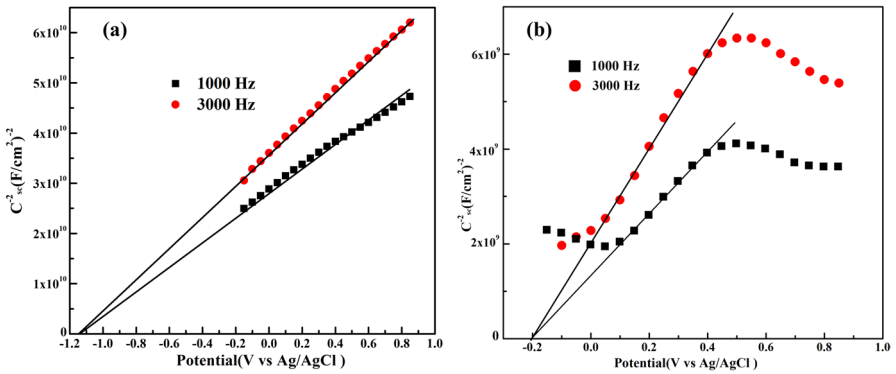

Fig. 8 Mott–Schottky plots of **a** SnO_2–Zn_2SnO_4 and **b** 10%Ag/SnO_2–Zn_2SnO_4. The experimental conditions include a Na_2SO_4 solution concentration of 0.2 mol/L and a scan rate of 5 mV/s at frequencies of 1000 and 3000 Hz

$$E_{CB} = E_{VB} - E_g \quad (3)$$

Here: E_{VB} is the valence band potential, E_{CB} is the conduction band potential, X is the electronegativity of the catalyst, E_e is the free electron potential (4.5 eV), and E_g is the bandgap energy.

The calculated CB potentials of SnO_2 and Zn_2SnO_4 are − 0.12 and − 0.4 eV, and their VB potentials are 3.62 and 3.44 eV.

In principle, due to their wide bandgap, SnO_2 and Zn_2SnO_4 cannot be excited to generate reactive oxygen species such as $\cdot O_2^-$ and ·OH under xenon lamp irradiation. Therefore, we proposed a Z-scheme model to generate a possible photocatalytic mechanism of the Ag/SnO_2–Zn_2SnO_4 composites. As displayed in Fig. S5, the incorporation of Ag metal and the presence of Sn vacancies in Zn_2SnO_4 (confirmed by XPS) extends the light absorption range of SnO_2 and Zn_2SnO_4 from UV to visible wavelengths [27, 34]. Upon excitation by visible light, electrons are transferred from the VBs of SnO_2 and Zn_2SnO_4 to their CBs, creating holes in the VBs. Since the bandgaps of these species match, the electrons are transferred from the CB of SnO_2 to the VB of Zn_2SnO_4 through the heterojunction interface and recombine with the holes. The photogenerated electrons simultaneously move from the CB of Zn_2SnO_4 to the Ag nanoparticles, where they are captured by O_2 in the reaction system, generating $\cdot O_2^-$ radicals, while the holes remaining in the VB of SnO_2 react with OH^- or H_2O to form ·OH radicals. This process effectively suppresses the rapid recombination of photogenerated electron–hole pairs, thereby enhancing the carrier lifetime. In addition, due to the local SPR effect, the Ag nanoparticles strongly absorb photon energy, which aligns with the absorption peak in the 400–500 nm region in the UV–Vis spectra. Consequently, this enhances the generation of photoproduced carriers on the Ag/SnO_2–Zn_2SnO_4 surface, leading to improved photocatalytic activity. In summary, the Ag/SnO_2–Zn_2SnO_4 composite exhibits a unique photocatalytic mechanism that leverages the band positions of its constituent materials to efficiently degrade Rh B under visible light irradiation.

Conclusions

Ag/SnO_2–Zn_2SnO_4 composite nanomaterials were prepared by chemical precipitation and photoreduction, with XRD, SEM, EDS, TEM, and XPS characterizations indicating their successful synthesis. According to the results, 10%Ag/SnO_2–Zn_2SnO_4 exhibited the highest photocatalytic performance in the degradation of Rh B, with a first-order kinetic rate constant of 0.1697 min^{-1}, more than twofold higher than that of SnO_2–Zn_2SnO_4. At the same time, the photocatalytic degradation of Rh B was maintained after five cycles, revealing the high photocatalytic stability of 10%Ag/SnO_2–Zn_2SnO_4. In short, the reinforced photocatalytic activity was attributed to the incorporation of metallic Ag, which not only captured photogenerated electrons to separate the carriers but also increased the capacity of visible light absorption to promote the generation of carriers.

Supplementary Information The online version contains supplementary material available at https://doi.org/10.1007/s11144-024-02682-2.

Acknowledgements The authors gratefully acknowledge financial support from the National Natural Science Foundation of China (22102069) and the Natural Science Foundation of Jiangxi Province (20224BAB213017).

References

1. Akhter P, Nawaz S, Shafiq I et al (2023) Efficient visible light assisted photocatalysis using ZnO/TiO_2 nanocomposites. Mol Catal 535:112896
2. Huang L, Bao D, Jiang X et al (2021) Fabrication of stable high-performance urchin-like CeO_2/ZnO@Au hierarchical heterojunction photocatalyst for water remediation. J Colloid Interface Sci 588:713–724
3. Nemiwal M, Zhang TC, Kumar D (2021) Recent progress in g-C_3N_4, TiO_2 and ZnO based photocatalysts for dye degradation: strategies to improve photocatalytic activity. Sci Total Environ 767:144896
4. Bolisetty S, Peydayesh M, Mezzenga R (2019) Sustainable technologies for water purification from heavy metals: review and analysis. Chem Soc Rev 48(2):463–487
5. Li J, Huang L, Jiang X et al (2021) Preparation and characterization of ternary Cu/Cu_2O/C composite: an extraordinary adsorbent for removing anionic organic dyes from water. Chem Eng J 404(2):127091
6. Chen H, Zhang YJ, He PY et al (2020) Coupling of self-supporting geopolymer membrane with intercepted Cr(III) for dye wastewater treatment by hybrid photocatalysis and membrane separation. Appl Surf Sci 515:146024
7. Ghoussoub YE, Fares HM, Delgado JD et al (2018) Antifouling ion-exchange resins. ACS Appl Mater Interfaces 10(48):41747–41756
8. Lu W, Junhe L, Lei L et al (2020) Effects of chloride on electrochemical degradation of perfluorooctanesulfonate by Magnéli phase Ti_4O_7 and boron doped diamond anodes. Water Res 170:115254
9. Aguilar SD, Ramos DR, Santaballa JA et al (2023) Preparation, characterization and testing of a bulky non-supported photocatalyst for water pollution abatement. Catal Today 413:113992
10. Pan Z, Ding W, Chen H et al (2024) A review on g-C_3N_4 decorated with silver for photocatalytic energy conversion. Chin Chem Lett 35(2):108567
11. Huang L, Yao J, Yang L et al (2022) Construction of Z-scheme $Bi_{12}O_{15}Cl_6$/SnO_{2-x} heterojunction for enhanced photocatalytic degradation of dyes and antibiosis. J Alloys Compd 908:164395
12. Zhang L, Yu W, Han C et al (2017) Large scaled synthesis of heterostructured electrospun TiO_2/SnO_2 nanofibers with an enhanced photocatalytic activity. J Electrochem Soc 164(9):H651–H656
13. Babu AT, Antony R (2022) Binary metal oxide nanocomposites of Fe, Co and Mn with SnO_2 for photodegradation of dyes, catalytic reduction of 4-nitrophenol and antimicrobial activities. React Kinet Mech Cat 135(1):539–553
14. Borker P, Salker A, Gaokar RD (2021) Sunlight driven improved photocatalytic activity of Mn doped SnO_2 nanowires. Mater Chem Phys 270:124797
15. Parthibavarman M, Sathishkumar S, Jayashree M et al (2019) Microwave assisted synthesis of pure and Ag doped SnO_2 quantum dots as novel platform for high photocatalytic activity performance. J Cluster Sci 30(2):351–363
16. Wang J, Fan H, Yu H (2015) Synthesis of monodisperse walnut-like SnO_2 spheres and their photocatalytic performances. J Nanomater 1:1–8
17. Malik R, Tomer VK, Rana PS et al (2015) Surfactant assisted hydrothermal synthesis of porous 3-D hierarchical SnO_2 nanoflowers for photocatalytic degradation of Rose Bengal. Mater Lett 154:124–127
18. Qu Y, Li Z, Sun N et al (2019) Visible-light induced electron modulation to improve photoactivities of coral-like Bi_2WO_6 by coupling SnO_2 as a proper energy platform. Catal Today 327:288–294
19. Kirubakaran K, Thangavel S, Nallamuthu G et al (2019) Enhanced photocatalytic degradation activity of 2-D graphitic carbon nitride-SnO_2 nanohybrids. J Nanosci Nanotechnol 19(6):3576–3582

20. Huang R, Huang S, Chen D et al (2019) Environmentally benign synthesis of Co_3O_4–SnO_2 heteronanorods with efficient photocatalytic performance activated by visible light. J Colloid Interface Sci 542:460–468
21. Zhang Y, Liu B, Chen N et al (2022) Synthesis of SnO_2/ZnO flowerlike composites photocatalyst for enhanced photocatalytic degradation of malachite green. Opt Mater 133:112978
22. Bathula B, Eadi SB, Lee H-D et al (2023) $ZnWO_4$ nanorod-colloidal SnO_2 quantum dots core@shell heterostructures: efficient solar-light-driven photocatalytic degradation of tetracycline. Environ Res 228:115851
23. Zhu Z, Xia H, Ren B et al (2023) Fabrication of solar-driven Zn_2SnO_4/g-C_3N_4 photocatalyst with enhanced photocatalytic performance for norfloxacin. Inorg Chem Commun 149:110432
24. Wang T, Wang X, Wang Y et al (2022) Construction of Zn_2SnO_4 decorated ZnO nanoparticles for sensing triethylamine with dramatically enhanced performance. Mater Sci Semicond Process 140:106403
25. Qi Y, Meador W, Xiong J et al (2021) Structural, optical, photocatalytic, and optoelectronic properties of Zn_2SnO_4 nanocrystals prepared by hydrothermal method. Nanotechnology 32(14):145702
26. Dong S, Cui L, Tian Y et al (2020) A novel and high-performance double Z-scheme photocatalyst ZnO–SnO_2–Zn_2SnO_4 for effective removal of the biological toxicity of antibiotics. J Hazard Mater 399:123017
27. Li Y, Wu X, Ho W et al (2018) Graphene-induced formation of visible-light-responsive SnO_2–Zn_2SnO_4 Z-scheme photocatalyst with surface vacancy for the enhanced photoreactivity toward NO and acetone oxidation. Chem Eng J 336(1):200–210
28. Zou X, Dong Y, Yuan C et al (2019) Zn_2SnO_4 QDs decorated Bi_2WO_6 nanoplates for improved visible-light-driven photocatalytic removal of gaseous contaminants. J Taiwan Inst Chem Eng 96:390–399
29. Wagh SS, Kadam VS, Jagtap CV et al (2023) Comparative studies on synthesis, characterization and photocatalytic activity of Ag doped ZnO nanoparticles. ACS Omega 8(8):7779–7790
30. Eka Putri A, Roza L, Budi S et al (2021) Tuning the photocatalytic activity of nanocomposite ZnO nanorods by shape-controlling the bimetallic AuAg nanoparticles. Appl Surf Sci 536:147847
31. Ma D, Shi J, Sun D et al (2019) Au decorated hollow ZnO@ZnS heterostructure for enhanced photocatalytic hydrogen evolution: the insight into the roles of hollow channel and Au nanoparticles. Appl Catal B Environ 244:748–757
32. Estrada-Vázquez R, Vaca-Mier M, Bustos-Terrones V et al (2024) Assessment of TiO_2 and Ag/TiO_2 photocatalysts for domestic wastewater treatment: synthesis, characterization, and degradation kinetics analysis. React Kinet Mech Cat 137(2):1085–1104
33. Bu X, Sun T, Liu Y et al (2024) Round-the-clock photocatalysis of plasmonic Ag-enhanced Z-scheme heterojunction material $Sr_2MgSi_2O_7$:(Eu, Dy)/g-C_3N_4@Ag under visible-light irradiation. Mol Catal 552:113674
34. Lu Q, Wei Z, Li C et al (2022) Photocatalytic degradation of methyl orange by noble metal Ag modified semiconductor Zn_2SnO_4. Mater Sci Semicond Process 138:106290
35. Liu J, Shu S, Li Y et al (2022) Ternary hybrid Ag/SnO_{2-X}/$Bi_4O_5I_2$ photocatalysts: impressive efficiency for photocatalytic degradation of antibiotics and inactivation of bacteria. Appl Surf Sci 606:154610
36. Jia T, Fu F, Long F et al (2016) Synthesis, characterization and enhanced visible-light photocatalytic activity of Zn_2SnO_4/C nanocomposites with truncated octahedron morphology. Ceram Int 42(12):13893–13899
37. Upadhaya D, Talinungsang KP et al (2019) Tuning the wettability and photocatalytic efficiency of heterostructure ZnO-SnO_2 composite films with annealing temperature. Mater Sci Semicond Process 95:28–34
38. Arora K, Kaur M, Singh H et al (2021) Sustainable preparation and enhanced photocatalytic activity of Ag/AgBr@G nanocomposite for degradation of water pollutants under visible light. Appl Surf Sci 553:149555
39. Onwudiwe DC, Gobile N, Oyewo OA et al (2023) Photocatalytic reduction of hexavalent chromium using Zn_2SnO_4–ZnO modified g-C_3N_4 composite. Results Eng 20:101521
40. Chen N, Liu B, Zhang P et al (2021) Enhanced photocatalytic performance of Ce-doped SnO_2 hollow spheres by a one-pot hydrothermal method. Inorg Chem Commun 132:108848
41. Cao X, Liu C, Li Q et al (2023) The research on photocatalytic oxygen evolution of $Bi_4Ti_3O_{12}$ microsphere by different Ag-loading content. Mater Lett 341:134219

42. Wu D, Sadaf S (2023) Sub-ppm level ethanol detection based on the gas sensor of g-C_3N_4–ZnO–Zn_2SnO_4 nanocomposite. Chem Phys Lett 817:140425
43. Li X, Chen D (2020) Hollow SnO_2 nanotubes decorated with $ZnIn_2S_4$ nanosheets for enhanced visible-light photocatalytic activity. J Alloys Compd 843:155772
44. Mahardika T, Putri NA, Putri AE et al (2019) Rapid and low temperature synthesis of Ag nanoparticles on the ZnO nanorods for photocatalytic activity improvement. Results Phys 13:102209
45. Guo Y, Zeng L, Xu X et al (2020) Regulating SnO_2 surface by metal oxides possessing redox or acidic properties: the importance of active O_2^-/O_2^{2-} and acid sites for toluene deep oxidation. Appl Catal Gen 605:117755
46. Liang D, Zhang X, Li Y et al (2023) Photocatalytic ipso-nitration of bromophenol intermediates on Ag/g-C_3N_4. Sustain Chem Pharm 33:101077
47. Zhang Q, Li Y, Zhong J et al (2023) Facile construction of CuO/g-C_3N_4 heterojunctions with promoted photocatalytic hydrogen generation behaviors. Fuel 353:129224
48. Li N, Miao S, Zheng X et al (2019) Construction of Ag_3PO_4/$BiNbO_4$ heterojunction photocatalysts with high activity for Rhodamine B removal under simulated sunlight irradiation. Ceram Int 45(18):24260–24268